



Cite this: *J. Mater. Chem. B*, 2017,
5, 3927

A novel nano-hybrid for cancer theranostics: folate sensitized Fe₂O₃ nanoparticles for colorectal cancer diagnosis and photodynamic therapy

Ramesh Nandi,^{†a} Snehasis Mishra,^{†b} Tuhin Kumar Maji,^a Krishnendu Manna,^b Prasenjit Kar,^a Saswati Banerjee,^b Shreyasi Dutta,^a S. K. Sharma,^c Peter Lemmens,^d Krishna Das Saha^{*b} and Samir Kumar Pal^{ib} ^{*a}

Organic–inorganic nano-hybrids are becoming popular for their potential biological applications, including diagnosis and treatment of cancerous cells. The motive of this study is to synthesise a nano-hybrid for the diagnosis and therapy of colorectal cancer. Here we have developed a facile and cost-effective synthesis of folic acid (FA) templated Fe₂O₃ nanoparticles with excellent colloidal stability in water using a hydrothermal method for the theranostics applications. The attachment of FA to Fe₂O₃ was confirmed using various spectroscopic techniques including FTIR and picosecond resolved fluorescence studies. The nano-hybrid (FA–Fe₂O₃) is a combination of two nontoxic ingredients FA and Fe₂O₃, showing remarkable photodynamic therapeutic (PDT) activity in human colorectal carcinoma cell lines (HCT 116) *via* generation of intracellular ROS. The light induced enhanced ROS activity of the nano-hybrid causes significant nuclear DNA damage, as confirmed from the comet assay. Assessment of p53, Bax, Bcl2, cytochrome c (cyt c) protein expression and caspase 9/3 activity provides vivid evidence for cell death *via* an apoptotic pathway. *In vitro* magnetic resonance imaging (MRI) experiments in folate receptor (FR) overexpressed cancer cells (HCT 116) and FR deficient human embryonic kidney cells (HEK 293) reveal the target specificity of the nano-hybrid towards cancer cells, and are thus pronounced MRI contrasting agents for the diagnosis of colorectal cancer.

Received 19th December 2016,
Accepted 22nd April 2017

DOI: 10.1039/c6tb03292c

rsc.li/materials-b

1. Introduction

Cancer has been considered to be a pestilential disease in the 21st century. Diagnosis of cancer and its treatment in an effective and affordable way is one of the exigent topics of modern research.^{1,2} The conventional treatment of cancer includes chemotherapy and surgery, which are painful and have several side effects which necessitate the search for other therapeutic strategies.³ Photodynamic therapy (PDT) has been an effective solution for the treatment of cancer, since its invention using hematoporphyrin by Dougherty *et al.* in 1975.⁴ In spite of the

potential and technical challenges, PDT is becoming an emerging solution for the treatment of cancer because of its noninvasive nature and selectivity.^{5–8} Administration of a drug followed by irradiation of light of an appropriate wavelength on the affected tissue excites the drug, which generates reactive oxygen species (ROS) and induces cell death.^{6,9–11} The target specific delivery of a drug in the case of PDT is the most important part for the efficacy of the treatment.⁹ In this regard, folic acid (FA) is a stable and cheap ligand that can target cancer cells *via* a folate receptor (FR).¹² Taking advantage of FRs targeting cancer cells is a well-known strategy due to overexpression of FR in a variety of cancer cells including those in breast, kidney, colon, ovaries, cervix and renal cell carcinomas.^{13–22} FA conjugated nano-materials such as Au nanoparticles (NPs), quantum dots and doped semiconductor were used for imaging or treatment of different FR+ cancer cells.^{17–20} Ligands, including FA, functionalized magnetic NPs are novel materials for their high colloidal stability, target specificity for important biomedical applications such as magnetic resonance imaging (MRI) and magnetic hyperthermia.^{22–31} FDA approved MRI contrast agents are gadolinium (Gd) based complexes, which lead to an emerging systematic disorder called nephrogenic systemic fibrosis (NSF).³² The development of a

^a Department of Chemical, Biological and Macromolecular Sciences, S. N. Bose National Centre for Basic Sciences, Block JD, Sector III, Salt Lake, Kolkata 700106, India. E-mail: skpal@bose.res.in; Fax: +91 33 2335 3477; Tel: +91 33 2335 5706-08

^b Cancer & Cell Biology Division, CSIR Indian Institute of Chemical Biology, Raja S.C. Mullick Road, Kolkata-700032, India. E-mail: krishna@iicb.res.in

^c Eko X-Ray & Imaging Institute, 54, Jawaharlal Nehru Road, Kolkata-700071, India

^d Institute for Condensed Matter Physics, and Laboratory for Emerging Nanometrology, TU Braunschweig Mendelssohnstrasse 3, 38106 Braunschweig, Germany

[†] These authors equally contributed to this work.

nontoxic MRI contrast agent as a diagnosis tool is a challenging job for researchers. Collaboration of therapeutics and diagnosis in a single nanomedicine can give a better prognosis. In recent times, theranostic nanomedicine has garnered increasing attention due to its simultaneous therapeutic and diagnosis capability.^{30,33,34} Nanomedicines having anticancer activity, selectivity for cancer cells and magnetic properties as a diagnosis tool have advantages over other medicines. Several approaches have been employed to synthesise folic acid functionalized iron oxide NPs for biomedical application using different organic linkers such as *N*-hydroxy-succinimide (NHS), 1-ethyl-3-(3-dimethylaminopropyl)-carbodiimide (EDC), 2,3-dibromopropionyl chloride (DBPC), polylactic-coglycolic acid and polyethylene glycol based attachment *via* a multi-step complicated method of synthesis, in which scaling up the synthesis is a big issue.^{16,22,30,35,36} Thus, the design of a simple one-step synthesis of FA templated iron oxide nanomedicines for theranostic applications is highly desirable.

In this work, we developed a simple one-step hydrothermal synthesis of folic acid templated water soluble magnetic iron oxide NPs (FA-Fe₂O₃). Structural and morphological characterization of the synthesized NPs was done using FESEM, TEM and XRD. Detailed spectroscopic characterization was performed with the help of FTIR, UV-Vis, fluorescence, and Raman spectroscopy and time correlated single photon counting (TCSPC). Picosecond resolved Förster resonance energy transfer (FRET) was used to confirm the attachment of FA to Fe₂O₃ at the molecular level. Photo-induced enhanced ROS generation of FA-Fe₂O₃ with respect to Fe₂O₃ was monitored by dichlorofluorescein (DCFH) oxidation. Magnetic property measurements were carried out using VSM study. Anti-cancer activity and cellular uptake studies were conducted on the human colorectal carcinoma (HCT 116) cell line. We have performed a relaxometry study and an MRI study of the synthesized FA-Fe₂O₃ to consider its potential use as a MRI contrast agent for diagnosis.

2. Experimental section

2.1. Reagents

Anhydrous FeCl₃, folic acid, dichlorofluoresceindiacetate (DCFH-DA) sodium dihydrogen phosphate (NaH₂PO₄) and sodium hydroxide (NaOH) were obtained from Sigma Aldrich. Ethanol and ethylene glycol were obtained from Merck. Chemicals used in this study were of analytical grade and used as received without further purification. HCT 116 (human colorectal carcinoma) cell line and HEK 293 (human embryonic kidney) cell lines were obtained from NCCS, Pune, India. Dulbecco's Modified Eagle's Medium (DMEM), penicillin/streptomycin/neomycin (PSN) antibiotic, fetal bovine serum (FBS), trypsin and ethylenediaminetetraacetic acid (EDTA) were obtained from Gibco-Life Technologies (Grand Island, NY, USA). Tissue culture plastic wares were purchased from NUNC (Roskilde, Denmark) from Fermentas, EU. 3-(4,5-Dimethylthiazol-2-yl)-2,5-diphenyltetrazolium bromide (MTT), DAPI (4',6-diamidino-2-phenylindole dihydrochloride), acridine orange and ethidium bromide were procured from SRL, (India), Invitrogen (California), Sigma-Aldrich (US), respectively. Antibodies

were bought from Santa Cruz Biotechnology, Inc. USA and eBioscience, Inc. San Diego, USA. Millipore water was used as an aqueous solvent. All other chemicals used were from Sigma-Aldrich Co. (St Louis, MO, USA).

2.2. Synthesis of Fe₂O₃

In our typical synthesis procedure, anhydrous FeCl₃ (203 mg) was dissolved in 5 ml ethylene glycol and the mixture was stirred for 30 min. Then, 15 ml 0.25 M NaOH was added dropwise with constant stirring. A brown colored precipitate was obtained. The resultant mixture then transferred into a Teflon-lined stainless-steel autoclave. The sealed autoclave was then kept at 150 °C for 18 h without stirring during the whole heating period. After completion of the reaction, the system was allowed to cool to ambient temperature naturally. The product was separated *via* centrifugation, washed three times with Millipore water and ethanol, respectively. The final product was dried on a water bath. Then the dried product was annealed at 550 °C for 1 h.

2.3. Synthesis of folic acid templated Fe₂O₃ (FA-Fe₂O₃)

Anhydrous FeCl₃ (203 mg) was dissolved in 5 ml ethylene glycol with constant stirring for 30 min followed by the dropwise addition of 5 ml of 0.25 M NaOH and the resultant solution was stirred for 30 min (denoted as solution A). Meanwhile, FA (27.6 mg) was dissolved in 5 ml of Millipore water and the pH was adjusted to ~7.4 using 0.1 M NaOH solution (denoted as solution B). Then solution B was added to solution A dropwise with constant stirring. The resultant mixture was stirred for 30 min and the pH was adjusted to ~7.4 using 0.25 M NaOH. Then the solution was transferred into a Teflon-lined stainless-steel autoclave. The sealed autoclave was then kept at 150 °C for 18 h without stirring during the whole heating period. After completion of the reaction, the system was allowed to cool to ambient temperature naturally. The product was separated *via* centrifugation, and washed three times with Millipore water and ethanol, respectively. The final product was dried on a water bath.

2.4. Characterization tools and techniques

Field emission scanning electron microscopy (FESEM, QUANTA FEG 250) investigations were performed by applying a diluted drop of NPs on a silicon wafer in order to investigate the surface morphology of the samples. Transmission electron microscopy (TEM) grids were prepared by applying a drop of dilute sample solution to carbon-coated copper grids. The particle sizes were determined from micrographs recorded at a magnification of 10⁵× using an FEI (Technai S-Twin, operating at 200 kV) instrument. The X-ray diffraction (XRD) patterns of the samples were recorded by employing a scanning rate of 0.02° S⁻¹ in the 2θ range from 20° to 80° using a PANalytical XPERTPRO diffractometer equipped with Cu Kα radiation (at 40 mA and 40 kV). Magnetic properties were measured in a Lake Shore vibrating sample magnetometer (VSM) with a field range of 0 to 1.6 T. For the Fourier transform infrared spectroscopy (FTIR), powdered samples were grinded with KBr powder and pelletized. The spectrum was recorded on a JASCO FTIR-6300 spectrometer.

The background correction was made by using a reference of KBr pellets. For optical experiments, steady-state absorption and emission were carried out with a Shimadzu UV-2600 spectrophotometer and a Jobin Yvon Fluorolog fluorimeter, respectively. A micro-Raman (Horiba LabRAM) setup with an excitation line of 532 nm was used in this study to record the Raman scattering spectra of all samples at room temperature. For picosecond-resolved spectroscopic studies, we followed the methodologies described in our earlier studies.^{37,38} Dynamic light scattering (DLS) measurements were performed using a NanoS Malvern instrument equipped with a 4 mW He:Ne laser ($\lambda = 632.8$ nm) and a thermostatted sample chamber. All the scattered photons were collected at a scattering angle of 173° . The scattering intensity data were processed using the software provided by the manufacturer to obtain the hydrodynamic diameter (d_H) and the size distribution of the scatterer in each sample. The instrument measures the time-dependent fluctuation in the intensity of light scattered from the particles in solution at a fixed scattering angle. d_H is defined as:

$$d_H = \frac{k_B T}{3\pi\eta D} \quad (1)$$

where k_B is the Boltzmann constant, T is the temperature, η is the viscosity, and D is the translational diffusion coefficient. In a typical size distribution graph obtained from the DLS measurements, the X-axis shows a distribution of size classes in nanometers, while the Y-axis shows the relative intensity of the scattered light. In all the ROS related extracellular and intracellular experiments, a 3 watt LED light has been used.

2.5. Förster resonance energy transfer (FRET) calculations

In order to determine the attachment of FA (donor) with Fe_2O_3 (acceptor), we used the following formulations.³⁹ The Förster distance (R_0) is given by

$$R_0 = 0.211 \times [\kappa^2 n^{-4} Q_D J(\lambda)]^{\frac{1}{6}} \text{ (In } \text{Å)} \quad (2)$$

where κ^2 is a factor describing the relative orientation in space of the transition dipoles of the donor and the acceptor. For donors and acceptors that randomize by rotational diffusion prior to energy transfer, the magnitude of κ^2 is assumed to be 2/3. The refractive index (n) of the medium is assumed to be 1.496. Q_D , the integrated quantum yield of the donor in the absence of an acceptor is ~ 0.005 . Molar extinction coefficients (ϵ_M) for FA are 6197 (363 nm) and 25 820 (280 nm).⁴⁰ Once the value of R_0 is known, the donor-acceptor distance (r_{DA}) can be easily calculated using the formula,

$$r_{DA}^6 = \frac{R_0^6 (1 - E)}{E} \quad (3)$$

where E is the efficiency of energy transfer and has been calculated following the procedure of our earlier work.³⁸

2.6. Preparation of DCFH for extracellular ROS generation study

DCFH was prepared by the deesterification reaction of DCFH-DA at room temperature.⁴¹ 0.5 ml of 1.0 mM DCFH-DA in

methanol was mixed with 2.0 ml of 0.01 N NaOH at room temperature for 30 min. Then the mixture was neutralized with 10 ml of 25 mM NaH_2PO_4 at pH 7.4. The resultant solution was kept at 4°C in the dark until use.

2.7. Cell culture and cytotoxicity assay

HCT 116 cells were cultured in DMEM supplemented with 10% fetal bovine serum (FBS) and 1% antibiotic (PSN) at 37°C in a humidified atmosphere under 5% CO_2 . After reaching 75–80% confluence, cells were harvested with 0.25% trypsin and 0.52 mM EDTA in phosphate buffered saline (PBS) and seeded at the required density to allow them to re-equilibrate for a day before starting the experiment. MTT assay was conducted to evaluate the cell viability. For the initial screening experiment, the HCT 116 cells (4×10^3 cells per well) were seeded in a 96 well plate and kept in an incubator followed by treatment with different concentrations of FA, Fe_2O_3 and FA- Fe_2O_3 (0.01 – $100 \mu\text{g ml}^{-1}$) for 24 h. The rest of our cellular study was carried out after treatment with a requisite amount of drug followed by 24 h incubation, unless mentioned otherwise. After 24 h of incubation, cells were rinsed with PBS, and then the MTT solution was added to each well and kept in an incubator for 4 h to form formazan salt. The formazan salt was then solubilized using DMSO and the absorbance was monitored at 595 nm using an ELISA reader (Emax, Molecular device, USA).⁴² Cell proliferation was determined from the absorption intensity. Cell viability was determined as follows

$$\text{Cell viability (\%)} = \frac{\text{OD}_{\text{control}} - \text{OD}_{\text{sample}}}{\text{OD}_{\text{control}}} \times 100 \quad (4)$$

The absorbance values of treated cells and untreated cells are denoted as $\text{OD}_{\text{sample}}$ and $\text{OD}_{\text{control}}$, respectively.

2.8. In vitro photodynamic therapy (PDT)

On the basis of preliminary screening experimentation on HCT 116 cells, $0.1 \mu\text{g ml}^{-1}$ concentration of FA- Fe_2O_3 was chosen for further experimentation, to check whether it exhibits any photosensitizing effect within the cells. Thus, $0.1 \mu\text{g ml}^{-1}$ of FA- Fe_2O_3 treated HCT 116 cells were exposed to blue light in a time-dependent manner (5, 10, 15, 30 and 45 min) following the MTT assay to determine the effectivity of photodynamic therapy.

2.9. Measurement of intracellular ROS generation using spectrofluorometry

Intracellular ROS accumulation was monitored using DCFH-DA, which is a well-known ROS marker. Briefly, the treated cells were incubated with $10 \mu\text{M}$ of DCFH-DA at 37°C for 25 min and then the cells were analyzed using a spectrofluorometer (JascoFP920, Hachioji, Tokyo, Japan).⁴³ Fluorescence intensity was monitored at 522 nm upon excitation at 488 nm.

2.10. Measurement of intracellular hydroxyl radical ($\cdot\text{OH}$) accumulation using flow cytometry

Intracellular hydroxyl radical ($\cdot\text{OH}$) accumulation was measured using hydroxyphenyl fluorescein (HPF), a specific indicator which reacts specifically with hydroxyl radicals. HPF exhibits bright

green fluorescence (excitation/emission maxima 490/515 nm) upon oxidation. The treated cells (2×10^6 cells) were incubated with HPF for 30 min in the dark followed by acquisition using a flow cytometer (BD LSRFortessa™ San Jose, CA, USA). The acquired data were analyzed using Flow Jo (Version 10.0) software.⁴⁴

2.11. Quantification of apoptosis using flow cytometry

Apoptotic and necrotic cell death was determined using the Annexin-V FITC/DAPI apoptosis detection kit (Calbiochem, CA, USA). Briefly, HCT 116 cells were pretreated with $0.1 \mu\text{g ml}^{-1}$ of FA-Fe₂O₃ followed by blue light exposure for different time durations (5, 10 and 15 min). Soon after light exposure, the cells were washed and stained with DAPI and Annexin-V-FITC in accordance with the manufacturer's instructions. The percentages of live, apoptotic (early and late) and necrotic cells were analyzed using a flow cytometer (BD LSRFortessa™ San Jose, CA, USA). The acquired data were analyzed using Flow Jo (Version 10.0) software.⁴⁵

2.12. Quantification of nuclear DNA in different phases of the cell cycle

HCT 116 cells were pretreated with FA-Fe₂O₃ ($0.1 \mu\text{g ml}^{-1}$) followed by blue light exposure for differential time durations (5, 10 and 15 min). After the treatment, the harvested cells were fixed overnight in 70% cold ethanol at 4 °C followed by centrifugation, resuspension in phosphate buffer saline (PBS) containing $25 \mu\text{g ml}^{-1}$ RNase and incubation for 1 h at 37 °C. Cells were then stained with propidium iodide (PI) ($50 \mu\text{g ml}^{-1}$) for 15 min at 4 °C. The stained nuclear DNA was analyzed using a flow cytometer (BD LSRFortessa™, San Jose, CA, USA).⁴⁵

2.13. Assessment of nuclear DNA damage using single cell gel electrophoresis assay

The oxidative DNA damage was assessed by performing the comet assay. The treated cells were mixed with 100 ml of 0.5% low melting agar (LMA) at 39 °C and then spread on a fully frosted microscopic slide pre-coated with 200 ml of 1% LMA. After agarose solidification, the slide was covered with 75 ml of 0.5% LMA and immersed in lysis solution (2.5 M NaCl, 100 mM Na-EDTA, 10 mM Tris, 1% TrionX-100 and 10% DMSO, pH 10) for 1 h at 4 °C. The slides were placed in a gel-electrophoresis apparatus containing 300 mM NaOH and 10 mM Na-EDTA (pH 13) for 40 min to allow DNA unwinding and the expression of alkali labile damage. An electrical field was applied (300 mA, 25 V) for 20 min at 4 °C to draw negatively charged DNA towards an anode. After electrophoresis, the slides were washed three times for 5 min at 4 °C in a neutralizing buffer (0.4 M Tris pH 7.5) and then stained with 75 ml ethidium bromide (EtBr) solution (20 mg ml^{-1}). The slides were photographed using a fluorescence microscope and the images were analyzed by Comet Score software (v1.5).⁴³

2.14. Analysis of protein expression by flow cytometry

Briefly, the treated cells were fixed with 4% paraformaldehyde in PBS (pH 7.4) for 20 min at room temperature. Then the cells

were permeabilized with 0.1% Triton X-100 in PBS along with 0.1% FBS for 5 min. The permeabilized cells were incubated with a primary antibody (p-p53^{Ser46}, Bax, Bcl2 and cytochrome *c*) for 2 h at 4 °C. The cells were then incubated with FITC-conjugated goat anti-rabbit IgG as a secondary antibody for 30 min at room temperature and washed in PBS before performing flow cytometry. The mean fluorescence intensities (MFI) were calculated using Flow Jo (Version 10.0) software.⁴⁶

2.15. Measurement of caspase 3 and caspase 9 activity

Caspase 3/9 activities were quantified according to the manufacturer's instructions with commercially available caspase 3 and caspase 9 colorimetric assay kits (BioVision Research Products, Mountain View, CA) respectively. Caspase activities were determined at 405 nm by an ELISA reader.⁴⁷

2.16. Determination of nuclear condensation and fragmentation using fluorescence microscopy

To detect nuclear damage or chromatin condensation, control cells with or without the treatment of FA-Fe₂O₃ ($0.1 \mu\text{g ml}^{-1}$) along with light exposure (15 min) were stained with acridine orange ($50 \mu\text{g ml}^{-1}$) and ethidium bromide ($50 \mu\text{g ml}^{-1}$) for 10 min. The images were acquired with an inverted phase contrast microscope (OLYMPUS IX 70, Olympus Optical Co. Ltd, Sibuya-ku, Tokyo, Japan) and the photographs were analyzed using ImageJ software. The emission was collected at 525 nm and 605 nm upon excitation at 488 nm.⁴⁸

2.17. *In vitro* cellular MR imaging studies of FA-Fe₂O₃

For cellular MR imaging, $\sim 6 \times 10^3$ numbers of HEK 293 and HCT 116 cells were incubated in a 96 well plate. Cells were treated with FA-Fe₂O₃ nanoparticles of concentrations 0.01–0.08 ng ml⁻¹ and kept for 8 h. Then cells were washed with PBS for three times and fixed using paraformaldehyde. To avoid air susceptibility 100 μL of 2% low melting agarose was added to each well. Then the plate was kept at 4 °C to solidify cell suspensions. MRI was performed keeping the samples under a 3T clinical MRI scanner (Siemens MAGNETOM Verio) using a pre-fabricated sample holder. MR phantom images were obtained by applying a spin-echo multi-section pulse sequence. In order to determine the transverse relaxation (T_2) of the sample, coronal images were taken at variable echo times (TE) of 13.2–212.8 ms with a repetition time (TR) of 1770 ms, an acquisition matrix of 209 mm \times 256 mm, a field of view of 208 mm \times 230 mm and a section thickness of 3 mm. The MRI signal intensity (SI) and visualization of the phantom images were analyzed using the standard software provided by the manufacturer.

2.18. Statistical analysis

Data were presented as mean \pm SEM. Statistical significance and differences among the groups were assessed *via* one-way analysis of variance (ANOVA) using OriginPro 8.0 software (San Diego, CA, USA). *p* value < 0.05 was considered as significant.

3. Results and discussion

3.1. Characterization of Fe₂O₃ and the FA-Fe₂O₃ nanohybrid

Fig. 1a and b depict the FESEM image of the as prepared Fe₂O₃ and FA-Fe₂O₃ respectively. Fe₂O₃ has a branched network-like morphology having a segment length of 300–500 nm and width of 50–70 nm. FA-Fe₂O₃ has a nano-egg-like morphology of length 150–200 nm and width 60–110 nm. Fig. 1c and d represents the corresponding HRTEM images of Fe₂O₃ and FA-Fe₂O₃, while insets show the corresponding HRTEM images at higher magnification. For both the samples, the fringe distance was

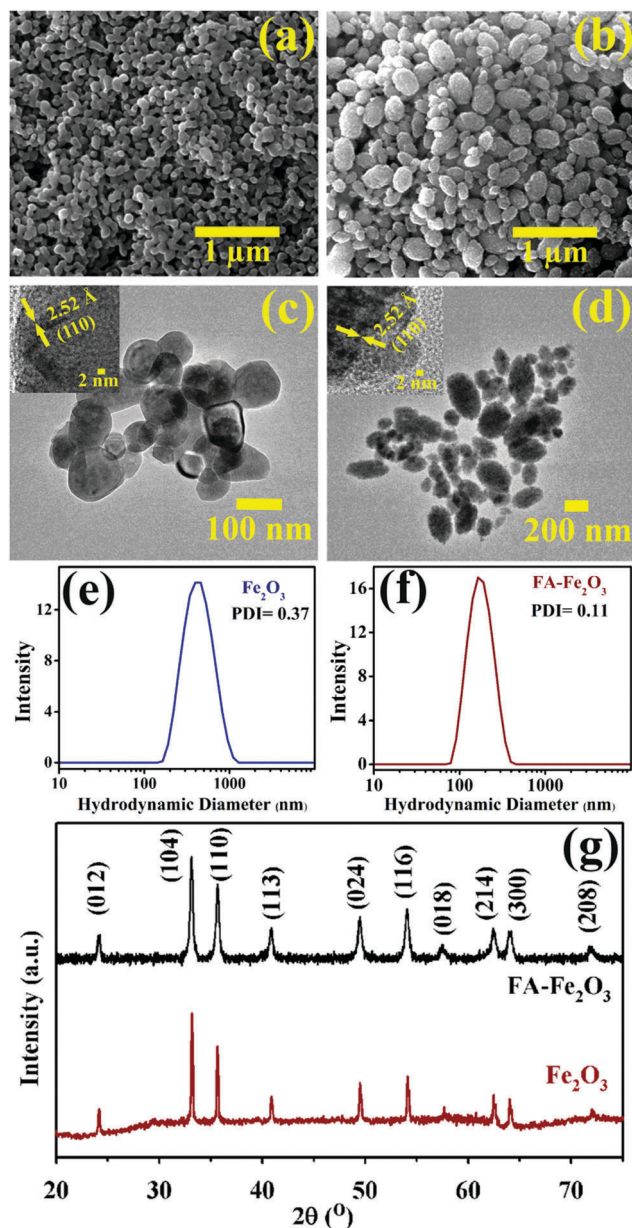


Fig. 1 FESEM image of (a) Fe₂O₃ and (b) FA-Fe₂O₃ NPs. HRTEM image of (c) Fe₂O₃ and (d) FA-Fe₂O₃ NPs. Inset of (c) and (d) shows the corresponding HRTEM images at higher magnification. Dynamic light scattering data of (e) Fe₂O₃ and (f) FA-Fe₂O₃ NPs dispersed in water. (g) XRD pattern of Fe₂O₃ and FA-Fe₂O₃ NPs.

found to be 2.52 Å which corresponds to the spacing between the (110) planes of α-Fe₂O₃.⁴⁹ The dynamic light scattering spectra of Fe₂O₃ and FA-Fe₂O₃ dispersed in water is shown in Fig. 1e and f. The hydrodynamic diameter for Fe₂O₃ and FA-Fe₂O₃ NPs was found to be 418 and 180 nm, respectively. The polydispersity index was found to be 0.37 and 0.11 for Fe₂O₃ and FA-Fe₂O₃ NPs respectively. The change in size and morphology of FA-Fe₂O₃ is due to the presence of FA. Here FA controls the morphology of FA-Fe₂O₃ NPs. The powder X-ray diffraction pattern of FA-Fe₂O₃ and Fe₂O₃ is shown in Fig. 1g. The diffraction pattern matches with the International Centre for Diffraction Data (ICDD) card no 33-0664, which corresponds to α-Fe₂O₃.⁴⁹ The XRD pattern and fringe distance from the HRTEM image imply that the crystal structure of α-Fe₂O₃ remains intact after FA templated synthesis.

Fig. 2a depicts the FTIR spectra of FA, Fe₂O₃ and FA-Fe₂O₃. Two sharp peaks at 472 cm⁻¹ and 550 cm⁻¹ are the characteristics of Fe–O stretching in the Fe₂O₃ spectrum. The lower frequency absorption remains unchanged but the higher one gets shifted to a higher frequency of 570 cm⁻¹ in FA-Fe₂O₃, which indicates a change in size during FA templated synthesis of Fe₂O₃.⁵⁰ The sharp peak at 1699 cm⁻¹ corresponds to the C=O stretching of the carboxylic acid group of FA. In FA-Fe₂O₃, the C=O stretching perturbed into two peaks, one remains at 1699 cm⁻¹ and another at 1684 cm⁻¹. This perturbation may be due to one of the free carboxylic acids of FA in FA-Fe₂O₃ and another one gets covalently attached with Fe₂O₃.⁵¹ The peaks in between 1485–1519 cm⁻¹ correspond to the phenyl and the pterin ring of FA.⁵² The Raman spectra of Fe₂O₃ and FA-Fe₂O₃ are shown in Fig. 2b. Fe₂O₃ has peaks at 228 cm⁻¹ and 500 cm⁻¹ corresponding to A_{1g} phonon modes and four E_g phonon modes at 248, 296, 413 and 612 cm⁻¹. Another 2 longitudinal optical (2LO) phonon modes are present at 1324 cm⁻¹.⁵³ The longitudinal optical (LO) phonon mode which is Raman forbidden is not observed in the case of Fe₂O₃.⁵³ But the LO phonon mode is observed in the case of FA-Fe₂O₃ at 662 cm⁻¹, the same mode was also observed by Onari *et al.*⁵⁴ This variation may be due to calcination at higher temperatures leading to better crystallinity of Fe₂O₃ than that of un-calcined FA-Fe₂O₃.⁵³

The differences in UV-Vis absorption spectra of Fe₂O₃ and FA-Fe₂O₃ are clearly depicted in Fig. 2c. FA has two well-known absorption bands at 360 and 280 nm.⁵⁵ Three possible electronic transitions are observed in the case of the Fe₂O₃ absorption spectra, absorption arising in the range of 200–400 nm is mainly due to ligand to metal charge transfer transition (LMCT) from oxygen to iron, the absorption band at 445 nm is attributed mainly to pair excitation from ⁶A₁ → ⁴E, ⁴A₁ of the magnetically coupled Fe³⁺–Fe³⁺ system and the sharp band at 568 nm is due to electronic transition from ⁶A₁ to ⁴T₂(⁴G) along with pair excitation of ⁶A₁ + ⁶A₁ → ⁴T₂(⁴G) + ⁴T₂(⁴G).^{56–58} In the case of FA-Fe₂O₃ the LMCT band is in the wavelength range 200–400 nm and the absorption band at 445 nm gets triggered; surprisingly the other one at 568 nm become sedate due to FA functionalization of Fe₂O₃. The significant spectral overlap of emission of FA with absorption of Fe₂O₃ has been shown in Fig. 2d. Steady state fluorescence quenching of FA was observed

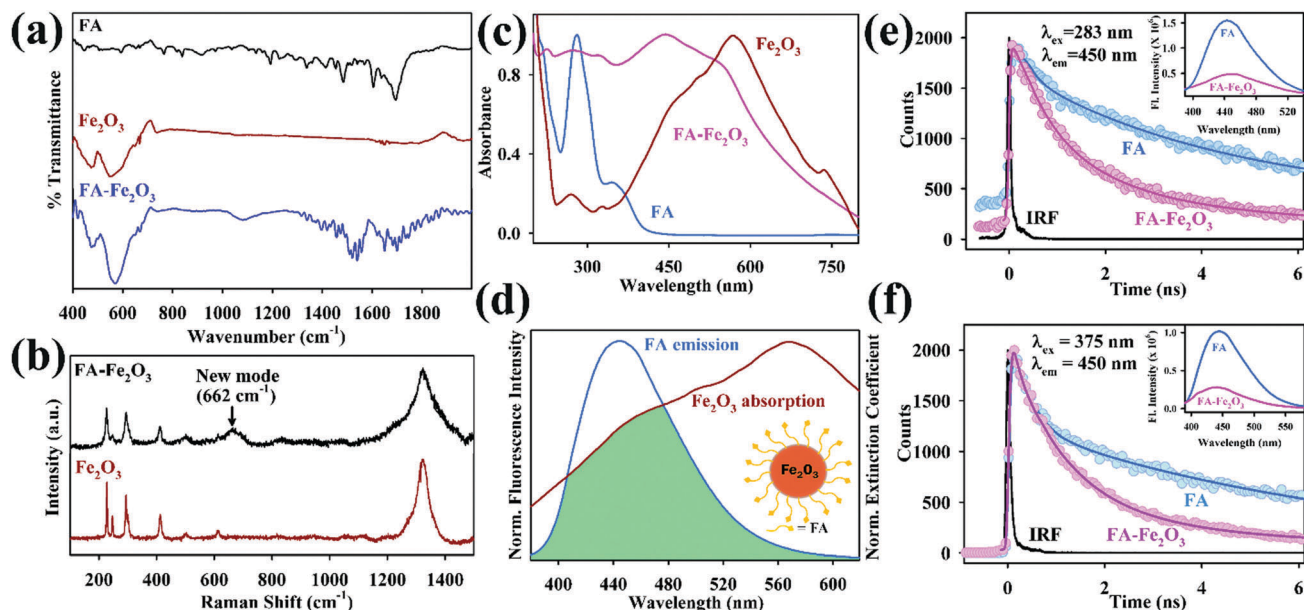


Fig. 2 (a) FTIR spectra of FA, Fe_2O_3 and FA- Fe_2O_3 . (b) Raman spectra of FA- Fe_2O_3 and Fe_2O_3 . (c) Absorption spectra of FA, Fe_2O_3 and FA- Fe_2O_3 . (d) Spectral overlap between emission of FA and absorption of Fe_2O_3 . (e) and (f) are the picosecond-resolved fluorescence transient spectra of FA in the absence and presence of Fe_2O_3 , recorded at 450 nm upon excitation at 283 nm and 375 nm, respectively. Insets show the corresponding steady state emission spectra.

in the presence of Fe_2O_3 upon excitation at 283 nm and 375 nm is shown in the insets of Fig. 2e and f, respectively. The steady state emission spectra of FA- Fe_2O_3 indicate that the structural integrity of FA remains unchanged after hydrothermal synthesis at 150 °C. It has been reported earlier that below 200 °C, FA exhibits water loss and degradation occurs after 200 °C.⁵⁹ Picosecond resolved fluorescent transients were recorded for both FA and FA- Fe_2O_3 at 450 nm upon excitation at 283 nm and 375 nm as shown in Fig. 2e and f, respectively and the corresponding time scales are tabulated in Table 1. We employed the well-known Förster resonance energy transfer (FRET) strategy to confirm the molecular level attachment of FA with Fe_2O_3 . The fluorescence lifetime of FA is found to be quenched in the presence of Fe_2O_3 NPs, which suggest a non-radiative energy transfer process from the donor (FA) to the acceptor (Fe_2O_3). The donor-acceptor distances (r_{DA}) have been calculated to be 1.11 nm and 1.13 nm for the excitation at 283 nm and 375 nm, respectively and all the other calculated FRET parameters are shown in Table 1. This molecular cross-talk between FA and Fe_2O_3 suggests an alteration in activities.

The colloidal stabilities of Fe_2O_3 and FA- Fe_2O_3 NPs dispersed in water were evaluated (Fig. 3a). The colloidal stability of FA- Fe_2O_3 was found to be ~ 40 times higher than Fe_2O_3 . The stability of FA- Fe_2O_3 in PBS solution was found to be more than 96 hours (data not shown here).

3.2. The study of magnetic properties

Magnetic properties measurements of FA- Fe_2O_3 using a vibrating sample magnetometer (VSM) shows magnetic field dependent magnetization (M vs. H) at 80 K and 300 K shows hysteresis features with coercivity 0.43 T and 0.053 T, respectively (Fig. 3d). The insets of Fig. 3d depict that the M_{ZFC} curve decreases and the M_{FC} rises slowly as a function of decreasing temperature revealing strong ferromagnetic properties and the blocking temperature was 332 K.

3.3. Extracellular ROS activity

In vitro ROS generation was evaluated using the well known DCFH assay, in which⁶⁰ DCFH is oxidized to fluorescent DCF by

Table 1 Lifetimes of picosecond-resolved fluorescent transient of FA and FA- Fe_2O_3 ^a

	System	λ_{ex} (nm)	λ_{em} (nm)	τ_1 (ns)	τ_2 (ns)	τ_3 (ns)	τ_{avg} (ns)
Picosecond resolved fluorescence transient lifetimes	FA	283	450	0.25 (35%)	4.50 (65%)	—	3.0
		375	450	0.28 (51%)	6.35 (49%)	—	3.3
	FA- Fe_2O_3	283	450	0.12 (14%)	0.78 (49%)	2.78 (37%)	1.4
		375	450	0.25 (33%)	1.30 (54%)	6.23 (13%)	1.6
	λ_{ex} (nm)	λ_{em} (nm)	$J(\lambda)$	E	r_{DA} (nm)		
FRET parameters of FA- Fe_2O_3	283	450	3.75×10^{13}	54.0	1.11		
	375	450	3.75×10^{13}	52.0	1.13		

^a The values in parentheses represent the relative weight percentages of the time components. The reported lifetimes carry $\sim 5\%$ uncertainties.

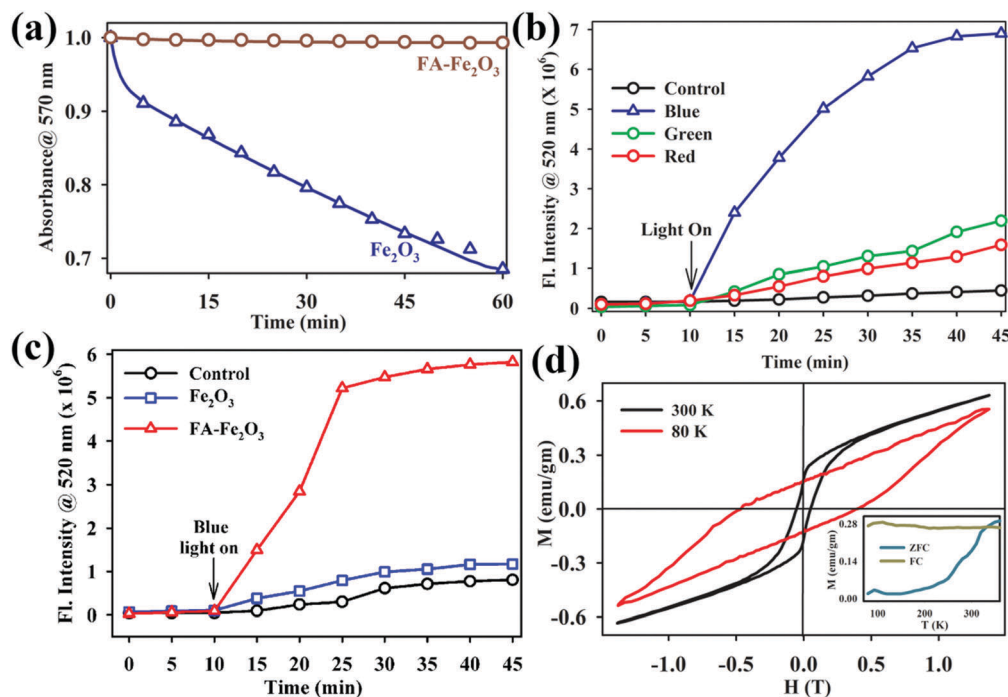


Fig. 3 (a) Colloidal stability of Fe₂O₃ and FA-Fe₂O₃ nanoparticles dispersed in water. (b) DCFH oxidation with respect to time in addition of FA-Fe₂O₃ and control in the dark and with subsequent light (red, green and blue) irradiation. (c) DCFH oxidation with respect to time in addition of Fe₂O₃, FA-Fe₂O₃, and control under dark with subsequent blue light irradiation. (d) Field dependent magnetization (M vs. H) of FA-Fe₂O₃ at 300 K and at 80 K. Bottom right inset shows temperature dependence of M_{ZFC} and M_{FC} curves measured at $H = 1.6$ T.

reacting with ROS and thus ROS generation was monitored using fluorescence of DCF at 520 nm. FA-Fe₂O₃ was assessed for its capability to generate ROS in the presence of a range of visible light excitation (blue: 460 ± 15 , green: 540 ± 15 and red: 640 ± 15 nm). Maximum ROS generation was observed in the presence of blue light (Fig. 3b). Blue light induced ROS generation is attributed mainly to the absorption band of Fe₂O₃ at 445 nm, which gets triggered after folic acid functionalization in FA-Fe₂O₃. This band is mainly responsible for enhanced ROS production through photoinduced electron-hole pair separation in FA-Fe₂O₃. We further evaluated ROS generation in the presence of Fe₂O₃ with control under blue light irradiation, which clearly reveals enhanced ROS generation in the case of FA-Fe₂O₃ (Fig. 3c). The swift nature of ROS generation gets saturated within 15 min, indicating a good signature for PDT application.

3.4. Cytotoxicity study

To check the cytotoxicity of the nanohybrid (FA-Fe₂O₃) and individual ingredients (FA and Fe₂O₃) HCT 116 cells were subjected to MTT assay without blue light exposure (Fig. 4a). HCT 116 cells were incubated with FA, Fe₂O₃ and FA-Fe₂O₃ of different concentrations (0.01, 0.1, 1, 10, 50 and 100 $\mu\text{g ml}^{-1}$). Native FA and Fe₂O₃ do not have significant cytotoxicity up to the concentration of 1 $\mu\text{g ml}^{-1}$. However, in the case of FA-Fe₂O₃, cell viability was reduced to 70.68% at the same concentration (Fig. 4a). After 1 $\mu\text{g ml}^{-1}$ concentration, the effect of FA-Fe₂O₃ on the cell viability of HCT 116 cells almost reached saturation. To determine the optimum cytotoxicity with the lowest concentration of FA-Fe₂O₃ in the absence of blue light,

another screening was done using FA-Fe₂O₃ of concentration up to 1 $\mu\text{g ml}^{-1}$. Fig. 4b depicts that the optimum cell viability was found to be 70.26% at 0.1 $\mu\text{g ml}^{-1}$ concentration of FA-Fe₂O₃. As folic acid, a well-known nutrient, does not have significant cytotoxicity, we have excluded folic acid from the next part of our cellular study.

3.5. FA-Fe₂O₃ mediated *in vitro* PDT in HCT 116 cell lines

Next, to ascertain the enhanced intracellular ROS activity of FA-Fe₂O₃ in the presence of blue light, HCT 116 cells were incubated with 0.1 $\mu\text{g ml}^{-1}$ of FA-Fe₂O₃ and were exposed to blue light for different time durations (5–45 min). A gradual decrease in the cell viability was observed with increase in blue light exposure time (in 5, 10, 15, 30 and 45 min of light exposure cell viability was 63.63%, 42.32%, 21.34%, 18.47% and 16.63%, respectively) as compared to the FA-Fe₂O₃ treated cells without light exposure (Fig. 4b and c). A light dose of 15 min shows maximum effect on cell death (cell viability 21.34%) and after that the effect is minimal, suggesting a rapid ROS activity of FA-Fe₂O₃ in HCT 116 cells, consistent with extracellular ROS generation. An *in vitro* PDT experiment illustrates the photodynamic effect of FA-Fe₂O₃ and also suggests a direct indication of photosensitized cytotoxicity of the FA-Fe₂O₃ nanohybrid in HCT 116 cells.

3.6. Intracellular ROS activity in the absence and presence of blue light

An intracellular ROS generation experiment was done using a cell permeable dye, DCFH-DA. HCT 116 cells were incubated

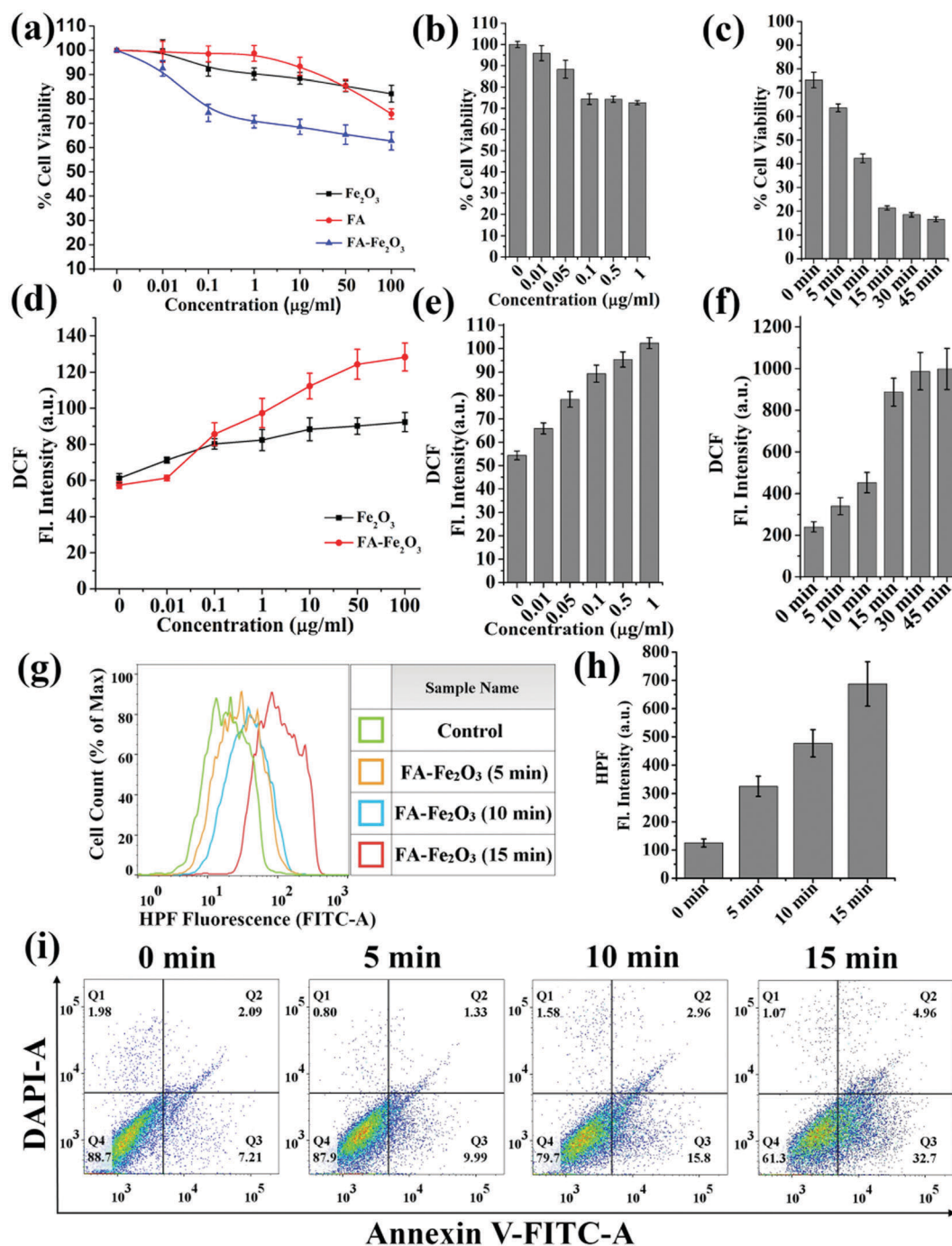


Fig. 4 HCT 116 cells were treated with the requisite amount of drugs for 24 h prior to various experiments. (a) MTT assay quantified cell viability with different concentrations of FA, Fe_2O_3 and FA- Fe_2O_3 in the absence of blue light. (b) The same at different concentrations of only FA- Fe_2O_3 . (c) Light induced cytotoxicity after treatment with $0.1 \mu\text{g ml}^{-1}$ of FA- Fe_2O_3 followed by blue light irradiation for different time durations (0–45 min). (d) Fe_2O_3 and FA- Fe_2O_3 treated dose dependent (0–100 $\mu\text{g ml}^{-1}$) intracellular ROS level in terms of DCF fluorescence intensity without blue light treatment. (e) FA- Fe_2O_3 treated dose dependent (0–1 $\mu\text{g ml}^{-1}$) intracellular ROS level in terms of DCF fluorescence intensity without blue light treatment. (f) Intracellular ROS measurement after treatment with $0.1 \mu\text{g ml}^{-1}$ FA- Fe_2O_3 followed by time dependent (0–45 min) blue light exposure. (g) Intracellular hydroxyl radical ($\cdot\text{OH}$) determination by HPF staining after treatment with FA- Fe_2O_3 followed by time dependent (0–15 min) blue light exposure, using flow cytometer. (h) Flow Jo analyzed data of hydroxyl radical ($\cdot\text{OH}$) determination. (i) Flow cytometric analysis of Annexin V-FITC/DAPI binding levels in FA- Fe_2O_3 ($0.1 \mu\text{g ml}^{-1}$) treated cells at different blue light exposure times.

with Fe_2O_3 and FA- Fe_2O_3 of different concentrations (0.01, 0.1, 1, 10, 50 and 100 $\mu\text{g ml}^{-1}$) to determine ROS activities without blue light exposure. As shown in Fig. 4d, Fe_2O_3 does not show

significant ROS activity without blue light exposure. Moreover, Fe_2O_3 shows minimal ROS activity in extracellular conditions (as shown in Fig. 3c) in the presence of blue light. Hence Fe_2O_3

have been excluded for further experiments. Fig. 4d depicts that FA-Fe₂O₃ treated cells shows moderate increase in DCF fluorescence intensity with respect to the Fe₂O₃ treated cells. Another screening was done in the absence of light with 0–1 μg ml⁻¹ of FA-Fe₂O₃. Fig. 4e depicts moderate intracellular ROS activity of the nanohybrid in the absence of blue light at a concentration of 0.1 μg ml⁻¹. Initial cytotoxicity studies showed that 0.1 μg ml⁻¹ of FA-Fe₂O₃ has an optimum effect on cell viability in the absence of blue light. To ascertain the intracellular ROS level in the presence of blue light with an optimum dose of FA-Fe₂O₃, the cells were treated with 0.1 μg ml⁻¹ FA-Fe₂O₃. The treated cells were exposed to blue light for different time durations (5, 10, 15, 30 and 45 min). Fig. 4f depicts that ROS generation was gradually increased upon increasing blue light exposure time (1.42-, 1.88-, 3.69-, 4.11- and 4.15-fold in 5, 10, 15, 30 and 45 min, respectively). The trend in intracellular ROS generation reached saturation with 15 min of light exposure, which is consistent with both extracellular ROS generation and photoinduced cytotoxicity assay. The considerable light induced enhanced intracellular ROS activity and optimum dark toxicity of 0.1 μg ml⁻¹ dose of FA-Fe₂O₃ indicates its potential in PDT.

3.7. Nature of intracellular ROS

Earlier reports have shown that amongst the numerous free radicals, the hydroxyl radical is commonly found cellular free radical that is produced through oxidative stress, and causes cell death.⁹ For the assessment of the type of ROS produced within the cell by light-sensitized FA-Fe₂O₃, a flow cytometric study of intracellular ROS generation was conducted using specific fluorescent probe HPF, a marker for hydroxyl radicals.⁴² Pretreated cells with 0.1 μg ml⁻¹ of FA-Fe₂O₃ were exposed to different light doses of 5, 10 and 15 min. A gradual ($p < 0.05$) increase in the HPF fluorescence intensity was observed (2.67-, 4-, 5.17-fold in 5, 10 and 15 min, respectively) with increasing light exposure time (Fig. 4g and h). The observation reveals that enhanced cytotoxicity upon blue light exposure is due to the

generation of hydroxyl radical within the cell in the presence of FA-Fe₂O₃.

3.8. FA-Fe₂O₃ induced apoptosis in HCT 116 cells

It is well known that phosphatidylserine (PS), a phospholipid component of cell membrane, is translocated in the membrane and externalized during apoptosis.⁴³ Annexin-V is a specific PS-binding protein that can be used to detect the apoptotic cells when conjugated with a specific fluorophore. On the other hand, the DNA binding dye DAPI was used along with annexin V to assess the degree of apoptosis and necrosis. To find out the underlying mechanism of the photodynamic effect of FA-Fe₂O₃ on HCT 116 cells, the flow cytometric technique was used using Annexin V-FITC/DAPI. The percentage viable cell population in FA-Fe₂O₃ treatment without light exposure was 88.7% following mild early apoptosis of 7.21%, late apoptosis of 2.09% and necrosis of 1.98%. Interestingly, the percentage of apoptotic (early and late) population increased progressively with the times of exposure (5, 10 and 15 min) of light in FA-Fe₂O₃ pretreated cells (Fig. 4i). With 15 min exposure of light, the viable cells were reduced to 61.3% following the enhancement of early/late apoptotic and necrotic population of 32.7%, 4.96% and 1.07%, respectively.

To further confirm the degree of apoptosis and necrosis upon treatment with FA-Fe₂O₃ in the presence of light, fluorescence microscopic analysis was conducted using a nuclear staining dye, AO and EtBr (Fig. 5a–j). Cells pretreated with FA-Fe₂O₃ had an intact nucleus with strong green AO fluorescence and weak red EtBr fluorescence (Fig. 5b and c). The scenario was reversed in the presence of light as shown in Fig. 5g and h, demonstrating clear nuclear fragmentation, which is also observed from the intensity curves (Fig. 5e and j).

3.9. Analysis of DNA content in sub-G0–G1 phase of the cell cycle

The estimation of fractional DNA content (sub-G0–G1) in the cell cycle is widely used as a marker to determine apoptosis.

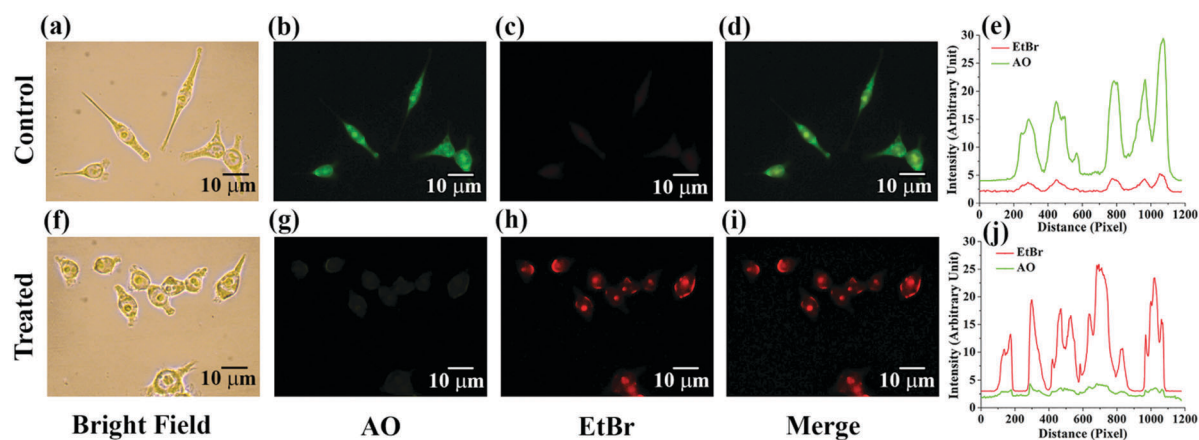


Fig. 5 Morphological changes of FA-Fe₂O₃ (0.1 μg ml⁻¹ for 24 h) treated HCT 116 cells followed by blue light exposure (15 min). (a) and (f) control and treated cells under bright field. (b) and (g) AO stained control and treated cells. (c) and (h) EtBr staining of control and treated cells. (d) and (i) Merged image of AO and EtBr stained cells. (e) and (j) Change in AO and EtBr fluorescence intensity of control and treated cells.

Thus, to investigate the PDT effect of FA-Fe₂O₃ on HCT 116 cells underlying the role of apoptosis, flow cytometric assessment of the percentage of DNA content in sub-G₀-G₁ phase of cell cycle was done (Fig. 6a). After treatment, the cells show the percentage of DNA content of 3.35% without any blue light exposure. After blue light exposure of different time durations (0–15 min) there was a significant enhancement in the percentage of DNA content (6.62, 9.03 and 13.52 percent in 5, 10 and 15 min, respectively) of sub-G₀-G₁ phase. The results demonstrate the role of fragmented

DNA regulating the apoptotic machinery in light induced FA-Fe₂O₃ mediated PDT.

3.10. FA-Fe₂O₃ induced nuclear DNA damage in HCT 116 cells

Nuclear DNA damage upon the blue light exposure on the FA-Fe₂O₃ treated cells was further confirmed by comet assay, which is a single cell gel electrophoresis assay for rapid and sensitive DNA damage. In the case of treated cells without blue

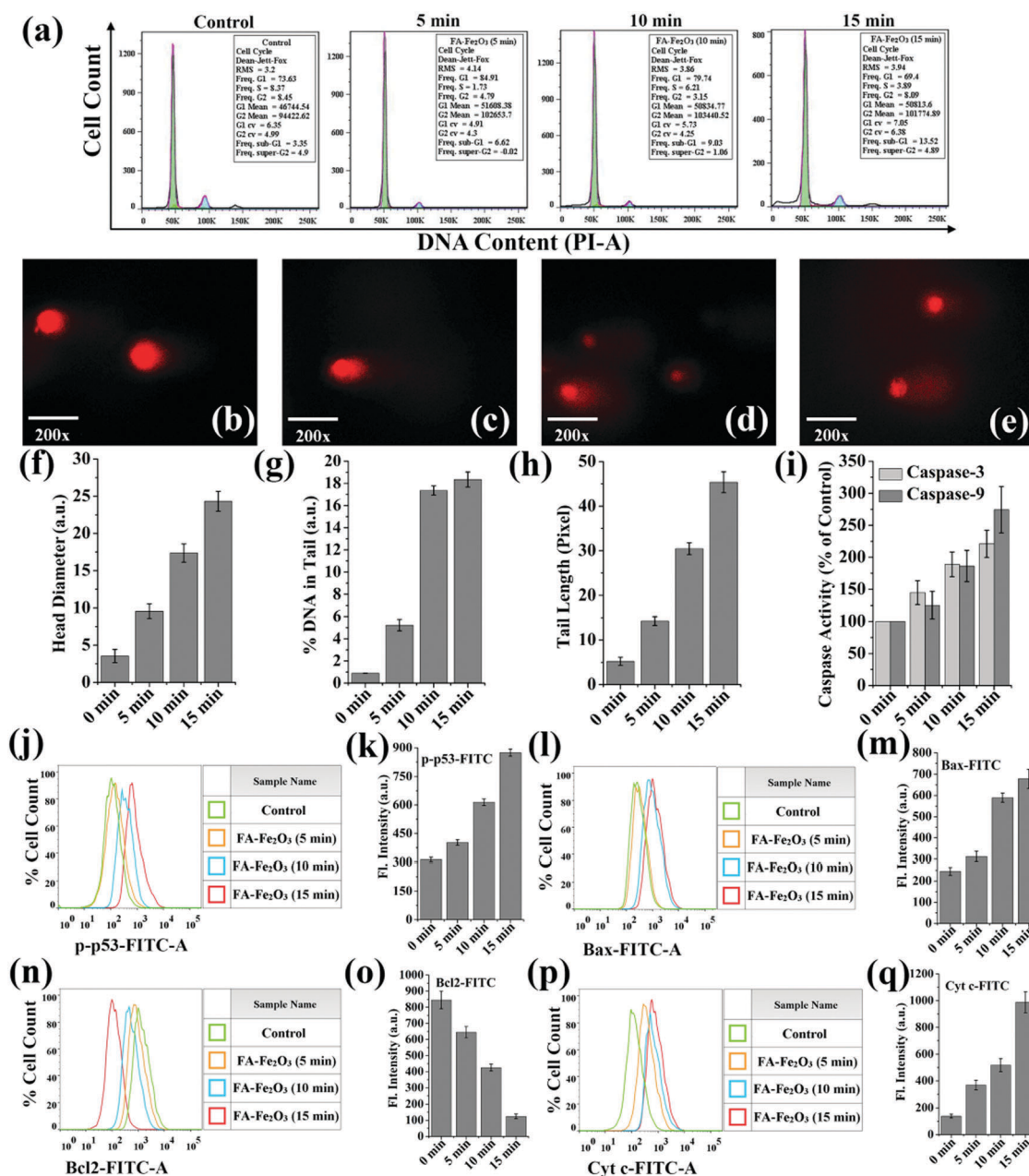


Fig. 6 HCT 116 cells were treated with requisite amount of FA-Fe₂O₃ for 24 h followed by time dependent blue light exposure prior to various experiments. (a) DNA content in sub-G₀-G₁ phase of the cell cycle. Representative microscopic images of comet assay. (b) Control. (c) 5 min. (d) 10 min. (e) 15 min blue light exposure. Comet score analyzed data of microscopic image obtained from comet assay experiment. (f) Head diameter. (g) % of DNA in tail. (h) Tail length. (i) Caspase 3 and caspase 9 activity. Analysis of (j) p53^{Ser46}, (l) Bax, (n) Bcl2, and (p) cytochrome c protein expressions, respectively. Flow Jo analyzed data of (k) p53^{Ser46}, (m) Bax, (o) Bcl2 and (q) cytochrome c protein expression, respectively.

light exposure, the migration of DNA from the origin was not significant, with increasing light exposure time, the tail length of damaged DNA increases, taking the shape of a comet (Fig. 6b–e). The head diameter in (2.70-, 4.90- and 6.87-fold in 5, 10 and 15 min, respectively), % DNA in tail (5.88-, 19.51- and 20.62-fold in 5, 10 and 15 min, respectively) and tail length (2.72-, 5.82- and 8.67-fold in 5, 10 and 15 min, respectively) were significantly ($p < 0.05$) increased with the gradual increase of blue light exposure time on FA-Fe₂O₃ treated cells. However, the absence of light exposure on FA-Fe₂O₃ treatment did not show any upliftment of DNA damage indices (head diameter, % DNA in tail and tail length) as compared to the light exposed treated cells (Fig. 6f–h). Light induced enhanced ROS generation damages nuclear DNA in HCT 116 cells.

3.11. FA-Fe₂O₃ upregulates the expression of phosphorylated p53 at Ser 46 in HCT 116 cells

Numerous studies have revealed that ROS act as upstream signal transducers for p53 activation and a downstream mediator of apoptosis.⁶¹ To understand the involvement of p53 phosphorylation in photosensitized apoptosis machinery, flow cytometric assessment was conducted in FA-Fe₂O₃-treated cells in the presence of blue light. Phosphorylation of the p53 expression significantly augmented with an increase in light dose duration to 5–15 min (Fig. 6j). As found in the flow cytometry analysis, the fluorescence intensity of p-p53-FITC was gradually ($p < 0.05$) increased (1.29-, 1.97- and 2.79-fold in 5, 10 and 15 min respectively) with respect to the FA-Fe₂O₃ treated control cell without any blue light exposure, indicating the correlation of ROS mediated p53 phosphorylation at Ser 46 in photodynamic therapy (Fig. 6k).

3.12. FA-Fe₂O₃ modulates the regulation of mitochondrial-dependent apoptosis machinery in HCT 116 cells

An altered level of pro/anti-apoptotic proteins, Bax, Bcl2 has been shown to regulate the mitochondrial-dependent apoptosis process through the modulation of phosphorylated p53 (Ser 46). Loss of function in anti-apoptotic Bcl2 triggers the release of cyt *c* to the cytosol in initiating the apoptotic cascade. To evaluate the detailed mechanism of FA-Fe₂O₃ induced apoptosis in the presence of blue light, flow cytometric assessment of mitochondria-dependent apoptosis regulating protein Bax, Bcl2 and cytochrome *c* was carried out (Fig. 6l, n and p). As shown in the flow cytometric histogram, the relative FITC fluorescence intensities of Bax (1.27-, 2.40- and 2.76-fold in 5, 10 and 15 min respectively) and cyt *c* (2.66-, 3.74- and 7.13-fold in 5, 10 and 15 min respectively) were gradually increased with increase in the duration of light treatment (Fig. 6l, m, p and q). On the other hand, the expression of anti-apoptotic Bcl2 was significantly ($p < 0.05$) suppressed (0.76-, 0.50- and 0.15fold in 5, 10 and 15 min respectively) with an increase in the duration of light treatment compared to without any light treatment (Fig. 6n and o). Therefore FA-Fe₂O₃ mediated PDT in HCT 116 cells initiate mitochondria-dependent apoptosis through p53 phosphorylation and are associated with a ROS mediated pathway.

3.13. FA-Fe₂O₃ enhances caspase 3/9 activation in HCT 116 cells

Caspase, a family of proteases, is responsible for triggering apoptosis by cleaving the specific enzymes. Upregulation of Bax/cytochrome *c* can induce caspase activation, which is responsible for initialization of apoptosis. Correlating with the data, a gradual augmentation of caspase 3/9 activity (1.45-, 1.89-, 2.21-fold in 5, 10 and 15 min, respectively for caspase 3 activity and 1.25-, 1.86- and 2.74-fold in 5, 10 and 15 min, respectively for caspase 9 activity) were found when the FA-Fe₂O₃ pretreated cells were exposed to blue light for different time durations (5, 10 and 15 min, Fig. 6i). Along with p53, Bax and Bcl2 protein expression caspase 3 and caspase 9 activity confirms that FA-Fe₂O₃ mediated PDT in HCT 116 cells induces cell death *via* an apoptotic pathway.

The nanohybrid FA-Fe₂O₃ possesses selectively blue light sensitized enhanced ROS activity. At an optimum concentration of 0.1 μg ml⁻¹ the nanohybrid possesses optimum dark toxicity and considerable light toxicity for the implementation of PDT. Upon blue light irradiation both in extracellular and intracellular conditions, FA-Fe₂O₃ rapidly generates ROS, which is found to be a hydroxyl radical from the HPF staining experiment (Fig. 4g and h). Light induced intracellular ROS generation causes nuclear DNA damage, which leads to increase in p53 protein expression inside the cell followed by upregulation of mitochondrial Bax protein and decrease in the Bcl2 protein level. The mitochondria started releasing cyt *c* leading to activation of pro-caspase 9 and pro-caspase 3 to caspase 9 and caspase 3 respectively, and ultimately cell death occurred *via* the apoptotic pathway.

3.14. MRI study

To test the potential applicability of FA-Fe₂O₃ as a diagnostic tool for cancer *in vitro* MRI study has been performed on HCT 116 cells along with HEK 293 cells as the control. Fig. 7a represents *T*₂ weighted phantom images of FA-Fe₂O₃ treated HEK 293 and HCT 116 cells. The signal intensity changes (from bright to dark) with an increase in the concentration of the FA-Fe₂O₃ (from 0.01 to 0.08 ng ml⁻¹) nanohybrid were observed in the case of HCT 116 compared to HEK 293 cells indicating targeted delivery of FA-Fe₂O₃ in FR overexpressed cells. The relaxivity plot (Fig. 7b) indicates a linear relation of the relaxation rate ($R_2 = 1/T_2$) with the nanohybrid concentration ($R_2 = 0.00184, 0.00267, 0.00452, 0.00557$ and 0.0077 msec⁻¹ for 0, 0.1, 0.2, 0.4 and 0.8 ng ml⁻¹ of FA-Fe₂O₃). With the increasing concentration of FA-Fe₂O₃, the transverse relaxation time (*T*₂) of the protons of water decreases and the relaxation rate (R_2) increases leading to darkening of the specific region of interest. This indicates that FA-Fe₂O₃ is a potential *T*₂ contrast agent.

Along with therapeutic properties FA-Fe₂O₃ also has potential MRI contrasting ability in HCT 116 cells. Shaoo *et al.* developed a FA conjugated silica coated manganese ferrite (FA-MSN) NPs for targeted delivery and MR imaging.⁶² FA-MSN shows MRI contrast at 0.05 mg ml⁻¹ concentration, whereas in the case of FA-Fe₂O₃ we found excellent contrast in cancer cells at 0.08 ng ml⁻¹, which has ~1000 times lower concentration with respect to the optimum dose found for the PDT. We observed a

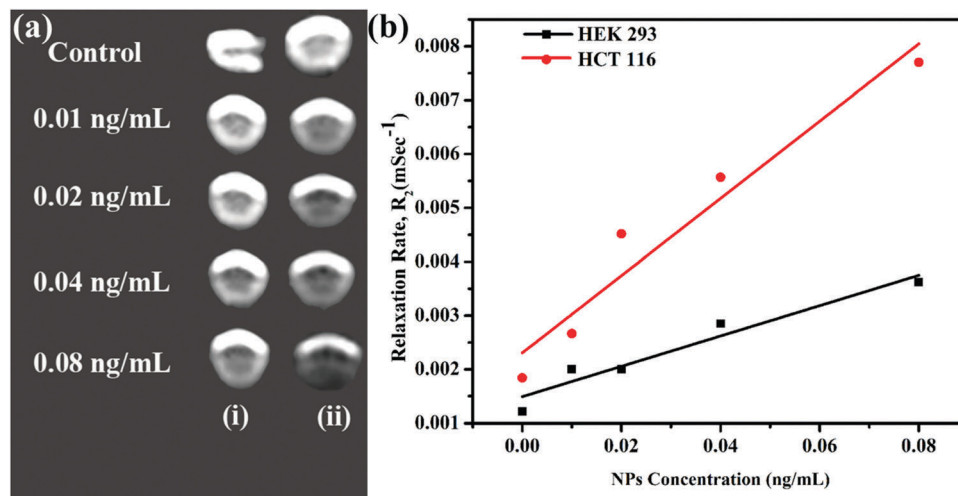


Fig. 7 (a) T_2 weighted MRI phantom images of (i) HEK 293 and (ii) HCT 116 cells treated with different concentrations of FA- Fe_2O_3 . (b) Relaxivity study of FA- Fe_2O_3 incubated in HEK 293 and HCT 116 cell lines.

pronounced MR contrast in FR+ cancer cells compared to FR deficient cells. FA mediated targeted delivery, light sensitized enhanced ROS activity and MRI contrasting competence of FA- Fe_2O_3 leads to a potential biomaterial for the dual application of diagnosis and therapy colorectal cancer.

4. Conclusion

In summary, we have developed a facile and cost-effective synthesis methodology of a novel nanohybrid (FA- Fe_2O_3), which demonstrates blue light sensitized target specific anti cancer activity in the human colorectal carcinoma cell line along with MRI contrasting abilities. Attachment of FA with Fe_2O_3 at the molecular level was confirmed from picosecond resolved fluorescence studies. Enhanced ROS activity was confirmed from extracellular and intracellular DCFH oxidation assay at different light exposure times. A cytotoxicity study in HCT 116 cells at different light exposure times reveals photoinduced enhanced cytotoxicity. Analysis of DNA content in the sub-G0-G1 phase of the cell cycle and comet assay reveals ROS mediated nuclear DNA damage in HCT 116 cells. ROS mediated cell death *via* the apoptotic pathway is evident from p53, Bax, Bcl2 and cytochrome *c* protein expression. Apoptosis mediated cell death was further confirmed from caspase 9 and caspase 3 activity. For diagnosis purposes *in vitro* MRI study reveals excellent contrast in FR overexpressed cancer cells (HCT 116) compared to FR deficient normal cells (HEK 293). Such blue light induced PDT can be done where affected tissues can be exposed to blue light using optical fibers (*e.g.* lung cancer, colorectal cancer, stomach cancer, throat cancer *etc.*). Finally, this work elicits a new approach towards the synthesis of effective, low cost nanohybrids for diagnosis and therapy of colorectal carcinoma.

Conflict of interest

There are no conflicts of interest to declare.

Acknowledgements

P. Kar thanks the Council of Scientific and Industrial Research (CSIR, India) for fellowship. T. K. Maji thanks of DST, INSPIRE for fellowship. We thank DAE (India) for financial grant 2013/37P/73/BRNS. We also thank DBT (India) for the financial grant (BT/PR11534/NNT/28/766/2014). PL thanks the NTH-School "Contacts in Nanosystems: Interactions, Control and Quantum Dynamics", the Braunschweig International Graduate School of Metrology, and DFG-RTG 1953/1, Metrology for Complex Nanosystems. We are thankful to Dr Sumita Kundu of Eko X-Ray & Imaging Institute, Kolkata for her kind help in executing the MRI experiment.

References

- N. C. S. Initiative, London, National Cancer Survivorship Initiative, 2013.
- R. Sullivan, O. I. Alatise, B. O. Anderson, R. Audisio, P. Autier, A. Aggarwal, C. Balch, M. F. Brennan, A. Dare and A. D'Cruz, *Lancet Oncol.*, 2015, **16**, 1193–1224.
- H. J. Burstein, *J. Clin. Oncol.*, 2000, **18**, 693.
- T. J. Dougherty, G. Grindey, R. Fiel, K. R. Weishaupt and D. Boyle, *J. Natl. Cancer Inst.*, 1975, **55**, 115–121.
- Z. Huang, H. Xu, A. D. Meyers, A. I. Musani, L. Wang, R. Tagg, A. B. Barqawi and Y. K. Chen, *Technol. Cancer Res. Treat.*, 2008, **7**, 309–320.
- D. Zhang, M. Wu, Y. Zeng, L. Wu, Q. Wang, X. Han, X. Liu and J. Liu, *ACS Appl. Mater. Interfaces*, 2015, **7**, 8176–8187.
- Z. Liu, X. Liu, Y. Du, J. Ren and X. Qu, *ACS Nano*, 2015, **9**, 10335–10346.
- E. Ju, K. Dong, Z. Chen, Z. Liu, C. Liu, Y. Huang, Z. Wang, F. Pu, J. Ren and X. Qu, *Angew. Chem.*, 2016, **128**, 11639–11643.
- Z. Hu, J. Li, C. Li, S. Zhao, N. Li, Y. Wang, F. Wei, L. Chen and Y. Huang, *J. Mater. Chem. B*, 2013, **1**, 5003–5013.

- 10 V. Morosini, T. Bastogne, C. Frochot, R. Schneider, A. François, F. Guillemin and M. Barberi-Heyob, *Photochem. Photobiol. Sci.*, 2011, **10**, 842–851.
- 11 Y.-P. Zeng, S.-L. Luo, Z.-Y. Yang, J.-W. Huang, H. Li, C. Liu, W.-D. Wang and R. Li, *J. Mater. Chem. B*, 2016, **4**, 2190–2198.
- 12 A. C. Antony, *Blood*, 1992, **79**, 2807–2820.
- 13 Y.-k. Lee, *Macromol. Res.*, 2006, **14**, 387–393.
- 14 P. Garin-Chesa, I. Campbell, P. Saigo, J. Lewis Jr, L. Old and W. Rettig, *Am. J. Pathol.*, 1993, **142**, 557–567.
- 15 A. R. Hilgenbrink and P. S. Low, *J. Pharm. Sci.*, 2005, **94**, 2135–2146.
- 16 F. Sonvico, S. Mornet, S. Vasseur, C. Dubernet, D. Jaillard, J. Degrouard, J. Hoebeke, E. Duguet, P. Colombo and P. Couvreur, *Bioconjugate Chem.*, 2005, **16**, 1181–1188.
- 17 C.-H. Wang, C.-W. Chang and C.-A. Peng, *J. Nanopart. Res.*, 2011, **13**, 2749–2758.
- 18 H. Meng, J.-Y. Chen, L. Mi, P.-N. Wang, M.-Y. Ge, Y. Yue and N. Dai, *J. Biol. Inorg. Chem.*, 2011, **16**, 117–123.
- 19 P. Suriamoorthy, X. Zhang, G. Hao, A. G. Joly, S. Singh, M. Hossu, X. Sun and W. Chen, *Cancer Nanotechnol.*, 2010, **1**, 19–28.
- 20 M. E. Mathew, J. C. Mohan, K. Manzoor, S. Nair, H. Tamura and R. Jayakumar, *Carbohydr. Polym.*, 2010, **80**, 442–448.
- 21 Y. Zhao, S. Liu, Y. Li, W. Jiang, Y. Chang, S. Pan, X. Fang, Y. A. Wang and J. Wang, *J. Colloid Interface Sci.*, 2010, **350**, 44–50.
- 22 J.-J. Lin, J.-S. Chen, S.-J. Huang, J.-H. Ko, Y.-M. Wang, T.-L. Chen and L.-F. Wang, *Biomaterials*, 2009, **30**, 5114–5124.
- 23 J. L. Arias, L. H. Reddy and P. Couvreur, *J. Mater. Chem.*, 2012, **22**, 7622–7632.
- 24 L. Li, M. Nurunnabi, M. Nafiujjaman, Y. Y. Jeong, Y.-k. Lee and K. M. Huh, *J. Mater. Chem. B*, 2014, **2**, 2929–2937.
- 25 B. C. Mei, K. Susumu, I. L. Medintz, J. B. Delehanty, T. Mountziaris and H. Mattoussi, *J. Mater. Chem.*, 2008, **18**, 4949–4958.
- 26 H. B. Na, G. Palui, J. T. Rosenberg, X. Ji, S. C. Grant and H. Mattoussi, *ACS Nano*, 2012, **6**, 389–399.
- 27 J. R. McCarthy and R. Weissleder, *Adv. Drug Delivery Rev.*, 2008, **60**, 1241–1251.
- 28 J. R. McCarthy, K. A. Kelly, E. Y. Sun and R. Weissleder, *Nanomedicine*, 2007, **2**, 153–167.
- 29 M. Sousa, J. Rubim, P. Sobrinho and F. Tourinho, *J. Magn. Magn. Mater.*, 2001, **225**, 67–72.
- 30 K. Hayashi, M. Moriya, W. Sakamoto and T. Yogo, *Chem. Mater.*, 2009, **21**, 1318–1325.
- 31 S. Bhandari, R. Khandelia, U. N. Pan and A. Chattopadhyay, *ACS Appl. Mater. Interfaces*, 2015, **7**, 17552–17557.
- 32 P. H. Kuo, E. Kanal, A. K. Abu-Alfa and S. E. Cowper, *Radiology*, 2007, **242**, 647–649.
- 33 Z. Medarova, W. Pham, C. Farrar, V. Petkova and A. Moore, *Nat. Med.*, 2007, **13**, 372–377.
- 34 Y. Liu, H. Miyoshi and M. Nakamura, *Int. J. Cancer*, 2007, **120**, 2527–2537.
- 35 A. J. Ditto, K. N. Shah, N. K. Robishaw, M. J. Panzner, W. J. Youngs and Y. H. Yun, *Mol. Pharmaceutics*, 2012, **9**, 3089–3098.
- 36 S. Mohapatra, S. Mallick, T. Maiti, S. Ghosh and P. Pramanik, *Nanotechnology*, 2007, **18**, 385102.
- 37 P. K. Sarkar, N. Polley, S. Chakrabarti, P. Lemmens and S. K. Pal, *ACS Sens.*, 2016, **1**, 789–797.
- 38 S. Choudhury, G. Naiya, P. Singh, P. Lemmens, S. Roy and S. K. Pal, *ChemBioChem*, 2016, **17**, 605–613.
- 39 J. R. Lakowicz, *Principles of Fluorescence Spectroscopy*, Kluwer Academic/Plenum, New York, 2nd edn, 1999.
- 40 D. M. Kranz, T. A. Patrick, K. E. Brigle, M. J. Spinella and E. J. Roy, *Proc. Natl. Acad. Sci. U. S. A.*, 1995, **92**, 9057–9061.
- 41 D. Bagchi, S. Chaudhuri, S. Sardar, S. Choudhury, N. Polley, P. Lemmens and S. K. Pal, *RSC Adv.*, 2015, **5**, 102516–102524.
- 42 M. Price, J. J. Reiners, A. M. Santiago and D. Kessel, *Photochem. Photobiol.*, 2009, **85**, 1177–1181.
- 43 I. Vermes, C. Haanen, H. Steffens-Nakken and C. Reutellingsperger, *J. Immunol. Methods*, 1995, **184**, 39–51.
- 44 D. J. Dwyer, M. A. Kohanski, B. Hayete and J. J. Collins, *Mol. Syst. Biol.*, 2007, **3**, 91.
- 45 A. Nandy, S. K. Dey, S. Das, R. N. Munda, J. Dinda and K. D. Saha, *Mol. Cancer*, 2014, **13**, 1.
- 46 K. Manna, U. Das, D. Das, S. Kesh, A. Khan, A. Chakraborty and S. Dey, *Free Radical Res.*, 2015, **49**, 422–439.
- 47 K. Manna, A. Khan, S. Biswas, U. Das, A. Sengupta, D. Mukherjee, A. Chakraborty and S. Dey, *RSC Adv.*, 2016, **6**, 23058–23073.
- 48 J. C. Kern and J. P. Kehrer, *Chem.-Biol. Interact.*, 2002, **139**, 79–95.
- 49 S. Chakrabarty, T. Jana, K. De, S. Das, K. Dey and K. Chatterjee, *Mater. Res. Express*, 2014, **1**, 046104.
- 50 Y. Wang, A. Muramatsu and T. Sugimoto, *Colloids Surf., A*, 1998, **134**, 281–297.
- 51 S. Dutta and B. N. Ganguly, *J. Nanobiotechnol.*, 2012, **10**, 1.
- 52 A. L. M. Raouf, K. K. Hammud, J. M. Mohammed and E. M. K. Al-Dulimy, *IJAPBC*, 2014, **3**, 773–780.
- 53 M. Massey, U. Baier, R. Merlin and W. Weber, *Phys. Rev. B: Condens. Matter Mater. Phys.*, 1990, **41**, 7822.
- 54 S. Onari, T. Arai and K. Kudo, *Phys. Rev. B: Condens. Matter Mater. Phys.*, 1977, **16**, 1717.
- 55 Y. Teow and S. Valiyaveetil, *Nanoscale*, 2010, **2**, 2607–2613.
- 56 D. M. Sherman and T. D. Waite, *Am. Mineral.*, 1985, **70**, 1262–1269.
- 57 S. Mitra, S. Das, K. Mandal and S. Chaudhuri, *Nanotechnology*, 2007, **18**, 275608.
- 58 S. Chakrabarty and K. Chatterjee, *J. Cryst. Growth*, 2013, **381**, 107–113.
- 59 L. Rojo, S. Radley-Searle, M. Fernandez-Gutierrez, L. M. Rodriguez-Lorenzo, C. Abradelo, S. Deb and J. San Román, *J. Mater. Chem. B*, 2015, **3**, 2708–2713.
- 60 S. Chaudhuri, S. Sardar, D. Bagchi, S. Dutta, S. Debnath, P. Saha, P. Lemmens and S. K. Pal, *ChemPhysChem*, 2016, **17**, 270–277.
- 61 Z. Gu, H. Wang, L. Li, Y. Liu, X. Deng, S. Huo, F. Yuan, Z. Liu, H. Tong and L. Su, *Sci. Rep.*, 2014, **4**, 4469.
- 62 B. Sahoo, K. S. P. Devi, S. Dutta, T. K. Maiti, P. Pramanik and D. Dhara, *J. Colloid Interface Sci.*, 2014, **431**, 31–41.